

Persistent Homology on Electron Backscatter Diffraction Data in Nano/ultrafine-grained Metallic Materials

Gong Na

The University of Tennessee

Nasrin Farzana

University of Hawaii at Manoa

Wang Yong

Nanyang Technological University

Wu Huibin

University of Science and Technology Beijing

Keffer David

The University of Tennessee

Maroulas Vasileios

The University of Tennessee

Rios Orlando (✉ orios1@utk.edu)

The University of Tennessee

Research Article

Keywords: Metallic materials, NG/UFG, EBSD, Schmid factor, PH

Posted Date: April 12th, 2021

DOI: <https://doi.org/10.21203/rs.3.rs-384380/v1>

License:   This work is licensed under a Creative Commons Attribution 4.0 International License.

[Read Full License](#)

Abstract

Nano/ultrafine-grained stainless steel was produced by severe cold deformation followed by annealing. The effect of annealing temperature on additional structural parameters, including the fraction of high-angle grain boundaries (HAGBs) and the kernel average misorientation (KAM), are revealed through electron backscatter diffraction. HAGB and KAM values provide a mechanistic understanding of the impact of structure on mechanical properties, including hardness, strength, and ductility. In this study, a novel application of persistent homology (PH) was employed to reduce the dimensionality of the information describing the complex processing-structure-property relationship. PH emphasizes the relationship between processing (annealing temperature), structure (distribution of the Schmid factor) and property (strength). Specifically, the PH formalism translates multidimensional data sets into clusters, distinguished by common PH features. In this analysis, two clusters emerge. First, at low annealing temperature, incomplete reversion of austenite results in materials with a greater fraction of grain boundaries, resulting in high strength and low ductility. Second, at high annealing temperature, fully reversed austenite results in lower, though still acceptable strength and superior ductility. The PH approach is applicable for identifying salient features in complex processing-structure-property relationships and is amenable to analysis of large data sets based on machine learning.

Introduction

Austenitic stainless steels with enhanced yield strength, good weldability and formability, and excellent corrosion resistance are widely used in various fields such as engineering applications and in everyday utensils¹⁻⁵. More recently, austenitic stainless steel is used as biomaterials to replace structural components of the human body because austenitic stainless steels possess superior tensile strength, fatigue strength, and fracture toughness⁶⁻⁹. A “top-down” approach, such as severe plastic deformation (SPD)^{10,11}, is a good way to obtain nanostructured materials from bulk coarse-grained materials. SPD is an effective procedure to obtain nanostructured materials with improved properties¹⁰. Techniques such as equal-channel angular pressing (ECAP), high-pressure torsion (HPT), accumulative roll-bonding (ARB) to achieve SPD have been proposed¹²⁻¹⁴. Materials fabricated via SPD techniques usually have a high strength-high ductility combination because of impurity free and porosity free properties^{15,16}. In the last ten years, a novel concept of phase reversion via severe cold reduction and subsequent annealing has been proposed to achieve nano/ultrafine-grained (NG/UFG) stainless steel with high strength and good ductility combination^{17,18}.

Orientation imaging microscopy (OIM) such as electron backscatter diffraction (EBSD) is a powerful technique which is used to characterize the spatial distribution of crystallographic orientation within a wide range of polycrystalline materials and associated microstructures¹⁹⁻²². In the last twenty years of the developments in the automated EBSD technique, it has become an important tool for quantitative metallography²³. Image analysis is one of the approaches to analyze plastic strain based on the effect of residual strain in the diffracting volume. Many factors such as grain boundaries, surface topology,

second phases, beam conditions, sample preparation, and camera settings affect image quality¹⁹. Also, a local misorientation approach is used to describe local variations in lattice orientation to identify dislocations in the material. The OIM measurement tool has the capability to allow a user to define different boundaries in maps created in OIM data. For example, OIM defines blue lines showing low angle grain boundaries with angles of 2–15° and high angle boundaries >15° in black. It is thought regions with higher concentrations of low angle boundaries (2–15°) have concentrated “geometrically necessary” dislocations density, where subgrain boundaries form¹⁹. Both kernel average misorientation (KAM), which captures the distribution of the dislocation density, as well as the Schmid factor of EBSD, which evaluates the ease of dislocation movement within a grain, are used to relate material structure and behavior^{21,22}. The EBSD technique can obtain the data required for quantitative microstructural analysis, especially the direct characterization of every crystal in a microstructure. This implies that EBSD can provide big data sets such as grain sizes and morphology of individual grains, crystallographic relationships between phases. While understanding these large data sets and building processing-microstructure-property relationships require the application of advanced analytical methods such as persistence homology (PH) and is compatible with artificial intelligence (AI) learning algorithm.

Geometry and topology rich areas of polycrystalline microstructures encompass patterns which may be difficult to analyze. By the same token, we propose a machine learning approach for deducing interesting patterns. Topological Data Analysis (TDA) utilizes topological tools to visualize and analyze data. Persistent homology (PH), the TDA’s popular workhorse, tracks changes in topological features at multiple scales. These features measure the differences between local and global critical regions of tensile strength across various temperatures. These differences are summarized in representations, called persistence diagrams (PDs)^{24–27}.

In this specific example, a novel application of the TDA mathematical framework is used to analyze the processing-structure-property relationships. The TDA mathematical framework is inherently sensitive to topological features was proposed to analyze the frequency distribution plot of the Schmid factor obtained from EBSD. First, we obtain a NG/UFG austenitic stainless steel with high-strength and good ductility combination. A series of EBSD measurements are conducted to analyze the microstructure and mechanical property in NG/UFG austenitic stainless steel. The PH method was used to find specific features, called (birth, death) points, to relate the Schmid factor frequency distribution plot to annealing temperature and mechanical strength.

Experimental

The chemical composition (wt%) of austenitic stainless steel 18Cr-8Ni is Fe–0.04C–1.52Mn–17.8Cr–8.1Ni–0.005P–0.005S. To obtain the NG/UFG structure, the solution-treated (1050 °C for 10-15 min) steel was subjected to severe cold reduction (80% reduction in thickness of ~1.5 mm) via multiple passes. Subsequently, the strips were cut to dimensions of 0.8 mm × 70 mm × 210 mm and annealed at temperatures ranging from 700 °C to 950 °C and the holding times were all 60 s when cold rolled martensite reverts to NG/UFG austenite.

The microstructures were examined using electron backscattered diffraction (EBSD). EBSD analyses were conducted using an HKL-Channel 5 system. The phase fractions were measured by X-ray diffraction (XRD). The mechanical properties of the reversion annealed specimens were determined by tensile testing via CMT5605 tensile machine with a 50 mm gage length and an HV-1000 micro-Vickers durometer at room temperature. Persistence diagrams (PDs) are generated from frequency distributions of Schmid factors by using sub-level set filtration library (gridDiag) of R package TDA.

Results And Discussion

Fig. 1 shows XRD patterns representing phase changes of samples annealed at different temperatures. In pattern solution treatment (ST) of Fig. 1, the solution-treated specimen has three austenite peaks, namely, $\gamma(211)$, $\gamma(110)$, and $\gamma(200)$, with 100% austenite content. After 80% cold rolling, strain-induced martensite was formed, with pattern 80% CR of $M(200)$ and $M(211)$ martensite peaks. Compared to the peaks of the solution-treated specimen, the martensite peaks increased dramatically, whereas the $\gamma(200)$, $\gamma(220)$, and $\gamma(311)$ austenite reflections drastically decreased. Subsequently, after annealing in the temperature range of 700 °C to 950 °C for 60 s, it is clear that martensite peak intensities decreased and austenite peak intensities increased gradually which indicated that the martensite reverted to austenite. In brief, at 700 °C, some weak martensite reflections were observed, which indicated the reversion was not complete. However, for patterns 800 °C, 850 °C, 950 °C of Fig. 1, few martensite peaks could be observed, which indicated the strain-induced martensite completely transformed into austenite. The volume fractions of the reversed austenite and martensite phases were calculated using MDI Jade 6.0. The results showed that the amount of reversed austenite increased with increasing annealing temperature. At 700°C, the volume fraction of reversed austenite was 65% with 35% martensite. At 750 °C, the volume fraction of reversed austenite was over 98%, and when the temperature was over 750 °C, the amount of reversed austenite was 100%.

Tensile tests were carried on the solution-treated and annealed specimens. Typical engineering stress-strain curves are shown in Fig. 2. The mechanical properties of austenitic stainless steels corresponding to five different annealing temperatures compared with solution-treated samples obtained via tensile tests are listed in Table 1. The hardness of samples is also presented in Table 1. It can be seen that the solution-treated sample shows low yield strength, σ_y , of 253 ± 22 MPa, the ultimate tensile strength, σ_t , of 733 ± 25 MPa and large elongation to fracture of $69.8 \pm 2\%$ with engineering stress-strain tensile curves shown in Fig. 2. The hardness of solution-treated sample is 183 ± 3 Hv. However, after annealing at 700 °C on 80% cold-rolled sample, the sample shows a high ultimate tensile strength of 1157 ± 16 MPa, high yield strength of 1028 ± 15 MPa and a low elongation of $8.2 \pm 1\%$ associated with engineering stress-strain tensile orange curve in Fig. 2. The hardness of 700 °C annealed sample is 376 ± 8 Hv. This is attributed to the existence of martensite (35%) after a low annealing temperature for a short time. When annealing temperature was increased, the tensile strength and hardness were both decreased, while the elongation increased. At an annealing temperature of 750 °C, the ultimate strength is 883 ± 10 MPa, yield strength is 562 ± 16 MPa, and hardness is 255 ± 5 Hv, while the elongation was significantly increased to

43.3 ± 1.5%, which is directly related to the stress-strain tensile curves C in Fig. 2. As the annealing temperature was increased to 850 °C, the ultimate tensile strength of steel has a few changes at 861 ± 14 MPa with a yield strength of 474 ± 2 MPa and hardness is 237 ± 2 Hv (stress-strain tensile red curve in Fig. 2). Meanwhile, the elongation was increased to a high value of 51.2 ± 2% (Table 1). At a higher annealing temperature of 950 °C, the ultimate strength decreased to 821 ± 10 MPa, yield strength was 337 ± 5 MPa, with hardness of 194 ± 5 Hv and high elongation of 62.5 ± 2.5% with stress-strain tensile pink curve in Fig. 2 extending to further distance as well as ST curve. From the mechanical properties of steels annealed at different temperatures (Table 1), it is clear that annealed temperature had a significant effect on austenitic stainless steel. The steel annealed in the temperature range of 750-850 °C exhibited a good combination of strength and ductility. Thus, it is necessary to analyze the microstructure in depth of annealed samples in order to understand the processing-structure-property relationship at work here.

Fig. 3 shows the EBSD maps of austenitic stainless steels annealed at different temperatures. The average grain size of these alloys is presented in Table 1. The average grain size of the solution-treated sample is 27 ± 8.5 µm. After the increase of annealing temperature, the samples showed nano/ultrafine-grained (NG/UFG) structure with increasing average grain size. The sample annealed at 700 °C has a small average grain size of 0.9 ± 0.4 µm (Fig. 3(b)). The white area in Fig. 3 is strain-induced martensite generated from severe cold rolling with residual stress which cannot be demarcated by EBSD. The reversed austenite is well demarcated by EBSD with different orientations showing in Fig. 3. When the annealing temperature was increased to 950 °C, the sample has a large average grain size of 11 ± 1.5 µm. This is attributed to austenite nucleated on martensite²⁸²⁹³⁰. After the reversion process was complete, the austenite grew, which influences the mechanical properties of the sample. It is clear that a higher fraction of grain boundaries with higher energies (i) contributes to the emission of dislocations from grain boundaries and (ii) suppresses grain boundary sliding, leading to a high strength³¹. Therefore samples annealed at low temperature have a higher strength because of a higher fraction of grain boundaries. The EBSD band contrast maps, which capture the grain boundary misorientation distribution of austenitic stainless steels at different annealing temperatures, are shown in Fig. 4. The blue lines and black lines represent the angle of misorientation below 15°, and above 15°, respectively. Misorientation greater than 15° results in high-angle grain boundaries (HAGB: black lines). Misorientation lower than 15° is designated low-angle grain boundaries (LAGB: blue lines). The fraction of HAGBs at different annealing temperatures was statistically generated using EBSD grain boundary misorientation maps and are presented associated with mechanical properties in Fig. 5. Higher fractions of HAGBs indicates more misorientation between neighboring grains and generate higher resistance against the disruption of grain boundaries by dislocations³². HAGBs can efficiently stop the propagation of brittle cleavage microcracks³³. However, LAGBs cannot prevent the glide of mobile dislocations. Grains with LAGBs can easily be rearranged into larger grains under deformation, which threatens the microstructural integrity and stability. Thus, it is clear that the volume fractions of LAGBs and HAGBs within the microstructure have significant influence on the stability and mechanical properties of materials³². The fraction of HAGBs increased from 52% to 86% with the annealing temperature changing from 700 °C to 950 °C. The HAGBs in austenitic stainless steels at higher annealing temperature prevent grains with LAGBs to nucleate or

the generation of microcracks, which exhibited higher ductility of NG/UFG steels. It is consistent with the observed experimental results. As exhibited in Fig. 5, the tensile strength and yield strength decreased with the increase of annealing temperature. The elongation of annealed samples increased from 8.2% to 62.5% with annealing temperature changing from 700 °C to 950 °C. Annealed samples with a higher fraction of HAGBs exhibited better ductility.

The kernel average misorientation (KAM), representing the average misorientation between neighboring points, was used to qualitatively evaluate the local dislocation density distribution^{19,21,22,34}. Neighboring grains with an orientation difference of 5° or larger, measured from the center, are excluded from the kernel²¹. It is known that low angle KAM (less than 1°) represents recrystallized material, whereas high angle KAM (greater than 1°) represents deformed material¹⁹. Since dislocations are mainly concentrated in deformed grains and sub-boundaries rather than subgrains and recrystallized grains, high KAM (greater than 1°) corresponds to deformed grains and lower KAM (less than 1°) to recrystallized grains^{21,22}. Fig. 6 shows KAM distribution maps of different annealed temperature samples. The white area in Fig. 6 is strain-induced martensite generated from severe cold rolling, which cannot be demarcated by EBSD. The maps show the KAM is divided into different ranges with blue regions representing the lowest KAM and red regions representing the highest KAM. Areas with net nonzero Burgers vectors have a change in crystallographic orientation or lattice curvature to satisfy geometrical compatibility between the grains and strain gradients due to geometrical constraints of the crystal lattice are often termed “geometrically necessary” dislocations (GNDs)^{19,35}. Fig. 6(f) shows the distribution of KAM values of different annealed temperature samples. It is clear that the maximum value of KAM values is lower with increasing annealing temperature, while the distribution of KAM broadens at higher annealing temperature (Fig. 6(a-e)). These results indicate that the dislocation density with little GNDs in reverted austenite was decreased with an increase of annealing temperature, which is consistent with the results of decreasing fraction of LAGB. When the recrystallization nucleates along deformed grains, namely, martensite reverted to austenite during annealing, the dislocation density decreased, and the resulting KAM value is low. These recrystallized grains nucleate from deformed grains, leading to the decrease of the dislocation density in recrystallized grains and the increase of ductility and decrease of hardness of NG/UFG material.

The Schmid factor is a parameter that characterizes the ease of activating dislocation movement within a grain²¹. “Hard” grains usually have a Schmid factor less than 0.35, while “soft” grains usually have a Schmid factor greater than 0.4. Soft grains, with high Schmid factors, slip more easily^{22,36}. Thus, deformation occurs easier in soft grains, resulting in lower yield strength²². Fig. 7 shows the Schmid factor of the same area of samples shown in Fig. 6. The colors in Fig.7 represent different values of Schmid factor, varying gradually with increasing annealing temperature. Blue regions represent the lowest Schmid factor and red regions represent the highest Schmid factor. In Fig. 7, all the samples have an average Schmid factor over 0.45, with higher Schmid factors corresponding to higher annealing temperature. A contour map is shown in Fig. 8 to better show the distributions of Schmid factor of different annealed samples associated with tensile strength. The color map in Fig. 8 represents the

relative frequency of Schmid factor. Purple and blue colors represent low relative frequency of Schmid factor and red colors represent high relative frequency of Schmid factor. Since the phase reversion is incomplete for samples annealed at 700 and 750 °C, there are missing parts (retained martensite) in EBSD maps. A red rectangle is used to identify a threshold greater than 5% contributing to the evaluation of the weighted arithmetic mean of the Schmid factor. The triangle symbol in Fig. 8 represents the weighted arithmetic mean of Schmid factor for each sample. It can be observed that nearly all the samples have an average Schmid factor over 0.45 and shifted to a higher Schmid factor value (dotted line) with a decrease of tensile strength (an increase of annealing temperature). It is consistent with the statement that softer materials have higher Schmid factor²². The second peak in Schmid number approaching 0.5 at high tensile strength (low annealing temperature) appears because it is sensitive to the absence of martensite area. The samples with high annealing temperature have higher Schmid factor where plastic deformation is easier to occur, leading to a good ductility and decrease of hardness of NG/UFG material.

Next, we analyzed the frequency distribution of Schmid factors for varying levels of annealing temperatures. By viewing the frequency distribution as a bounded continuous function of Schmid factor, the sublevel set filtration tracks the evaluation of connected components in sets, as, a frequency value, approaches from a local minimum to a local maximum. The key idea is that as increases the connectivity of sets remain unchanged except when it passes through critical points (maxima and minima in a sublevel set). For example, in Fig. 9, the frequency plot of Schmid factor at an annealing temperature of 50 °C is presented. In Fig. 9, we use reference (blue dashed) lines to present the growth of. As we increase the value of, the reference line moves upward. In Fig. 9(a) left for a small value we observe two connected components (red color segments) in the sublevel set and we track their evolution (as shown in Fig. 9(a) right). These two connected components have the same birth scale (λ). When the value reaches to the level of Fig. 9(b) left another connected component (shown in green) is born and we record the birth of that component. We keep tracking the growth of these connected components in the right figure of 9(b). The two connected components (left red and green) merged when the reference line of growing reaches the level shown in Fig. 9(c) left. According to the *Elder rule*³⁷, when two components merge the one born later disappears and the one born earlier persists. Hence the green component should disappear as shown in Fig. 9(c) right. By paring the two points, the value of when the green connected component is born and the value of when it merges with the red connected component, as coordinates of a two-dimensional plot, we obtained a point in the persistence diagram (PD) as shown in green in Fig. 9(f). That is to say, the red connected component that is born earlier will continue to grow and be joined with a later local maximum. The last connected component appears in Fig. 9(d) and is shown in purple. This one quickly merges with the red connected component on the left and produces a point in the corresponding PD (purple point in Fig. 9(f)). Once we reach the reference line corresponding to the value of, all the sublevel sets are merged into a single connected component and we terminate the procedure (Fig 9(e)). For every connected component that arises in the filtration we plot the pair or in the PD, where is the value of at which the component is born and is the value when it dies.

In Fig. 10 we superimposed PDs generated from frequency distributions of Schmid factors as shown in Fig. 7. Typically, the points in PDs with low death coordinate corresponds to noise or insignificant features, whereas those with higher death coordinate corresponds to topologically significant characteristics of the dataset. This showcases the usefulness of this exploratory tool for investigating the Schmid factor in a compact and informative way. As softer materials have higher Schmid factors²², our samples with high annealing temperature were observed to have higher Schmid factors. The PD generated from the Schmid factor frequency distribution at low annealing temperature (700 and 750 °C) shows several higher death values (red rectangles and green circle in Fig. 10) which indicates the samples have several levels of Schmid factors. This is consistent with the results in Fig. 7. The death value of pair in PDs represents the highest frequency of Schmid factor in a sublevel Schmid factor set. The high death values of samples annealed at 700 and 750 °C implied that distribution of Schmid factor has large difference due to the incomplete phase reversion (nonuniform distribution as well as martensite). Whereas, with a higher annealing temperature, the phase reversion was complete with 100% austenite, so we observed only one point with high death value in the corresponding PDs (for example the blue, pink and brown symbols in Fig. 10).

We present the correlation of Schmid factor frequency distribution and PDs in Fig. 11. The rectangle on the left side figure represents the birth to death lifetime. The arrow represents the direction of birth to death lifetime. The related color in the right side dot represents the generated connected component. There are two different kinds of connected components marked in Fig. 11. In brief, the red marker in Fig. 11 (left) exhibits the lifetime of the highest frequency of Schmid factor in the whole Schmid factor set. And the direction of the lifetime is always from left to right. The black marker in Fig. 11 (left) exhibits the lifetime of the highest frequency of Schmid factor in a sublevel Schmid factor set (the length of the rectangle). The red dot marker is the generated connected component related to the red rectangle. The white dot maker is the generated connected component related to the black rectangle. In summary, the left side of Fig. 11 contour maps showing the shift of Schmid factor frequency under different annealing temperatures. The right side of Fig. 11 contour maps exhibit the fluctuation of the Schmid factor frequency. The more connected components identified in Fig. 11, the greater the noise and volatility of the Schmid factor frequency, which is consistent with EBSD analysis.

One important function of persistent homology analysis in a TDA framework is to accentuate meaningful data and help eliminate data imperfections that can obscure accurate evaluation and development of complex correlations. EBSD analysis reveals two sources of error or noise. The first is correlated to the stochastic natural variability of the sample itself. Another source of imperfection is the measurement error of the instrument and discretizing of a continuous distribution during post-processing that is used to quantify the Schmid factor and crystallographic information.

Beyond acting as a statistical filter, the value of the PH analysis is to reduce the dimensionality of the information describing the processing-structure-property (PSP) relationship, so that significant relationships become apparent. In this work, the integration of the PH analysis and the material characterization emphasizes the relationship between processing (annealing temperature), structure

(distribution of the Schmid factor) and property (tensile strength). In a comparison of Fig. 11(a) and Fig. 11(b) as well as Fig. 11(c) and Fig. 11(d), the complex contour plot of Fig. 11(a) and Fig. 11(c) are rendered into a series of 5 white dots in Fig. 11(b) and Fig. 11(d), respectively, which can visually be grouped into two distinct categories, one corresponding to low annealing temperature (700-800 °C) and the other containing materials with higher annealing temperature (850-950 °C). As is marked in Fig. 11, the blue oval represents the recrystallization phase of materials. While the yellow oval represents the recrystallized grains have grown up to a coarsening state. The red oval represents the highest frequency of Schmid factor in the whole sublevel Schmid factor set which always has a connected component born at 0 with the highest death value. Conceptually analogous to a Principal Component Analysis, the PH analysis provides the ability to group established categories of materials based on commonalities in their processing-structure-property relationships.

The PH analysis does not change the nature of conclusions. Rather the PH analysis makes the PSP relationship more obvious to the untrained eye. This approach is amenable to machine learning from large convoluted data sets that obscure analysis based on direct observation.

Conclusions

In summary, a nano/ultrafine-grained (NG/UFG) austenitic stainless steel was obtained via 80% severe cold deformation and annealing in the 700-950°C for 60 s. In the temperature range of 750-850 °C, austenitic stainless steel exhibited a good combination of strength and ductility. Orientation imaging microscopy techniques, including EBSD band contrast, kernel average misorientation and Schmid factor were used to perform crystallography analysis of microstructure and mechanical properties of austenitic stainless steel annealed at different temperatures. Samples annealed at low temperature have a higher percentage of grain boundaries which contributed to the strength of NG/UFG steel. The EBSD band contrast, kernel average misorientation and Schmid factor values explained a good ductility and decrease of hardness of annealed NG/UFG austenitic stainless steel. A novel PH method was used to emphasize dominant features in the processing-structure-property relationship of these stainless steels. The PH method can be applied to a wide range of data sets and distributions, not just Schmid factor distributions, as shown here.

Declarations

Acknowledgments

Many thanks to the Tickle College of Engineering, Department of Materials Science and Technology, University of Tennessee, Knoxville, and partnership relating to this work. Valuable discussion with Professor R.D.K. Misra is gratefully acknowledged.

Author contributions

Gong N, Rios O and Wu H conceived the idea; Gong N and Wang Y performed the experiments and conducted the characterization of materials; Maroulas V and Farzana N performed the persistence homology calculations; Gong N, Rios O, Wang Y, Wu H, Maroulas V, Farzana N contributed to the correction of the manuscript; Gong N and Rios O contributed to the application of PH in relationship among processing, structure, and properties; Rios O and Keffer DJ revised the manuscript written by Gong N. All the authors commented on the manuscript.

Conflict of Interest

There are no conflicts of interest associated with this publication and there is no significant financial support for this work that could have influenced its outcome.

References

1. Haanappel, V. A. C. & Stroosnijder, M. F. Influence of mechanical deformation on the corrosion behavior of AISI 304 stainless steel obtained from cooking utensils. *Corrosion***57**, 557–565 (2001).
2. Kaladhar, M., Subbaiah, K. V. & Rao, C. S. Machining of austenitic stainless steels - A review. *Int. J. Mach. Mach. Mater.***12**, 178–192 (2012).
3. Huang, G. L., Matlock, D. K. & Krauss, G. Martensite formation, strain rate sensitivity, and deformation behavior of type 304 stainless steel sheet. *Metall. Mater. Trans. A***20**, 1239–1246 (1989).
4. Challa, V. S. A., Wan, X. L., Somani, M. C., Karjalainen, L. P. & Misra, R. D. K. Strain hardening behavior of phase reversion-induced nanograined/ultrafine-grained (NG/UFG) austenitic stainless steel and relationship with grain size and deformation mechanism. *Mater. Sci. Eng. A***613**, 60–70 (2014).
5. Gong, N., Wu, H. B., Yu, Z. C., Niu, G. & Zhang, D. Studying Mechanical Properties and Micro Deformation of Ultrafine-Grained Structures in Austenitic Stainless Steel. *Metals (Basel)***7**, 188 (2017).
6. Sumita, M., Hanawa, T. & Teoh, S. H. Development of nitrogen-containing nickel-free austenitic stainless steels for metallic biomaterials. *Mater. Sci. Eng. C***24**, 753–760 (2004).
7. Stolyarov, V. V., Zhu, Y. T., Lowe, T. C., Islamgaliev, R. K. & Valiev, R. Z. A two step SPD processing of ultrafine-grained titanium. *Nanostructured Mater.***11**, 947–954 (1999).
8. Murphy, W., Black, J. & Hastings, G. W. (Eds.). *Handbook of biomaterial properties*. (Springer, 2016).
9. Kuroda, D., Kawasaki, H., Hiromoto, S. & Hanawa, T. Annual Book of ASTM Standards, Section 13, Medical Devices and Services Annual Book of ASTM Standards, Section 13, Medical Devices and Services, 2000. *Mater. Trans.***46**, 1532–1539 (2005).
10. Valiev, R. Nanostructuring of metals by severe plastic deformation for advanced properties. *Nat. Mater.***3**, 511–516 (2004).
11. Zhu, Y. T. & Langdon, T. G. The fundamentals of nanostructured materials processed by severe plastic deformation. *Jom***56**, 58–63 (2004).

12. Huang, C. X. *et al.* Bulk nanocrystalline stainless steel fabricated by equal channel angular pressing. *J. Mater. Res.***21**, 1687–1692 (2006).
13. Valiev, R. Z., Alexandrov, I. V. & Islamgaliev, R. K. Processing and properties of nanostructured materials prepared by severe plastic deformation. in *Nanostructured materials*. Springer, Dordrecht 121–142 (Springer, 1998).
14. Valiev, R. Z., Korznikov, A. V. & Mulyukov, R. R. Structure and properties of ultrafine-grained materials produced by severe plastic deformation. *Mater. Sci. Eng. A***168**, 141–148 (1993).
15. Jiang, H., Zhu, Y. T., Butt, D. P., Alexandrov, I. V. & Lowe, T. C. Microstructural evolution, microhardness and thermal stability of HPT-processed Cu. *Mater. Sci. Eng. A***290**, 128–138 (2000).
16. Sumita, M., Ikada, Y. & Tateishi, T. Metallic Biomaterials-Fundamentals and Applications. in *ICP, Tokyo* 629 (2000).
17. Misra, R. D. K., Challa, V. S. A., Venkatsurya, P. K. C., Shen, Y. F., Somani, M. C., Karjalainen, L. P. Interplay between grain structure, deformation mechanisms and austenite stability in phase-reversion-induced nanograined/ultrafine-grained austenitic ferrous alloy. *Acta Mater.***84**, 339–348 (2015).
18. Misra, R. D. K. *et al.* Phase reversion induced nanograined austenitic stainless steels: microstructure, reversion and deformation mechanisms. *Mater. Sci. Technol.***29**, 1185–1192 (2013).
19. Wright, S. I., Nowell, M. M. & Field, D. P. A Review of Strain Analysis Using Electron Backscatter Diffraction. *Microsc. Microanal.***17**, 316–329 (2011).
20. Adams, B. L., Wright, S. I. & Kunze, K. Orientation imaging: the emergence of a new microscopy. *Metall. Trans. A***24**, 819–831 (1993).
21. Chen, P. *et al.* In-situ EBSD study of the active slip systems and lattice rotation behavior of surface grains in aluminum alloy during tensile deformation. *Mater. Sci. Eng. A***580**, 114–124 (2013).
22. Li, J., Li, H., Liang, Y., Liu, P. & Yang, L. The Microstructure and The Microstructure and Mechanical Properties of Multi-Strand, Composite Welding-Wire Welded Joints of High Nitrogen Austenitic Stainless Steel. *Materials (Basel)*.**12**, 2944 (2019).
23. Humphreys, F. J. Grain and subgrain characterisation by electron backscatter diffraction. *J. Mater. Sci.***36**, 3833–3854 (2001).
24. Maroulas, V., Nasrin, F. & Oballe, C. A bayesian framework for persistent homology. *SIAM J. Math. Data Sci.***2**, 48–74 (2020).
25. Townsend, J., Micucci, C. P., Hymel, J. H., Maroulas, V. & Vogiatzis, K. D. Representation of molecular structures with persistent homology for machine learning applications in chemistry. *Nat. Commun.***11**, 1–9 (2020).
26. Spannaus, A. *et al.* Materials Fingerprinting Classification. *arXiv Prepr. arXiv2101.05808* (2021).
27. Maroulas, V., Mike, J. L. & Oballe, C. Nonparametric Estimation of Probability Density Functions of Random Persistence Diagrams. *J. Mach. Learn. Res.***20**, 1–49 (2019).

28. Misra, R. D. K., Nayak, S., Mali, S. A., Shah, J. S., Somani, M. C., Karjalainen, L. P. Microstructure and deformation behavior of phase-reversion-induced nanograined/ultrafine-grained austenitic stainless steel. *Metall. Mater. Trans. A Phys. Metall. Mater. Sci.***40**, 2498–2509 (2009).
29. Gong, N. *et al.* Effect of martensitic transformation on nano-ultrafine-grained structure in 304 austenitic stainless steel. *J. Iron Steel Res. Int.***24**, 1231–1237 (2017).
30. Gong, N., Wu, H. B., Niu, G. & Zhang, D. Effects of annealing temperature on nano/ultrafine-grained structure in austenite stainless steel. *Mater. Sci. Technol. (United Kingdom)***33**, 1667–1672 (2017).
31. Wang, Y., Fu, R., Jing, L., Sang, D. & Li, Y. Tensile behaviors of pure copper with different fraction of nonequilibrium grain boundaries. *Mater. Sci. Eng. A***724**, 164–170 (2018).
32. Canadinc, D., Biyikli, E., Niendorf, T. & Maier, H. J. Experimental and numerical investigation of the role of grain boundary misorientation angle on the dislocation–grain boundary interactions. *Adv. Eng. Mater.***13**, 281–287 (2011).
33. Lambert-Perlade, A., Gourgues, A. F. & Pineau, A. Austenite to bainite phase transformation in the heat-affected zone of a high strength low alloy steel. *Acta Mater.***52**, 2337–2348 (2004).
34. Saraf, L. Kernel average misorientation confidence index correlation from FIB sliced Ni-Fe-Cr alloy surface. *Microsc. Microanal.***17**, 424–425 (2011).
35. Ariza-Echeverri, E. A. *et al.* Development of a new generation of quench and partitioning steels: Influence of processing parameters on texture, nanoindentation, and mechanical properties. *Mater. Des.***186**, 108329 (2020).
36. Gussev, M. N., Field, K. G. & Busby, J. T. Deformation localization and dislocation channel dynamics in neutron-irradiated austenitic stainless steels. *J. Nucl. Mater.***460**, 139–152 (2015).
37. Edelsbrunner, H. & Harer, J. *Computational topology: an introduction*. (American Mathematical Soc., 2010).

Tables

Table 1 Mechanical properties of stainless steel.

Steels	Average grain size/ μm	σ_t /MPa	σ_y /MPa	Elongation/%	HV
solution-treated	27 \pm 8.5	733 \pm 25	253 \pm 22	69.8 \pm 2	183 \pm 3
700 °C /60 s	0.9 \pm 0.4	1157 \pm 16	1028 \pm 15	8.2 \pm 1	376 \pm 8
750 °C /60 s	1.6 \pm 0.4	883 \pm 10	562 \pm 16	43.3 \pm 1.5	255 \pm 5
800 °C /60 s	2.5 \pm 0.6	867 \pm 13	522 \pm 12	49.0 \pm 1	257 \pm 7
850 °C /60 s	3.6 \pm 0.5	861 \pm 14	474 \pm 2	51.2 \pm 2	237 \pm 2
950 °C /60 s	11 \pm 1.5	821 \pm 10	337 \pm 5	62.5 \pm 2.5	194 \pm 5

Figures

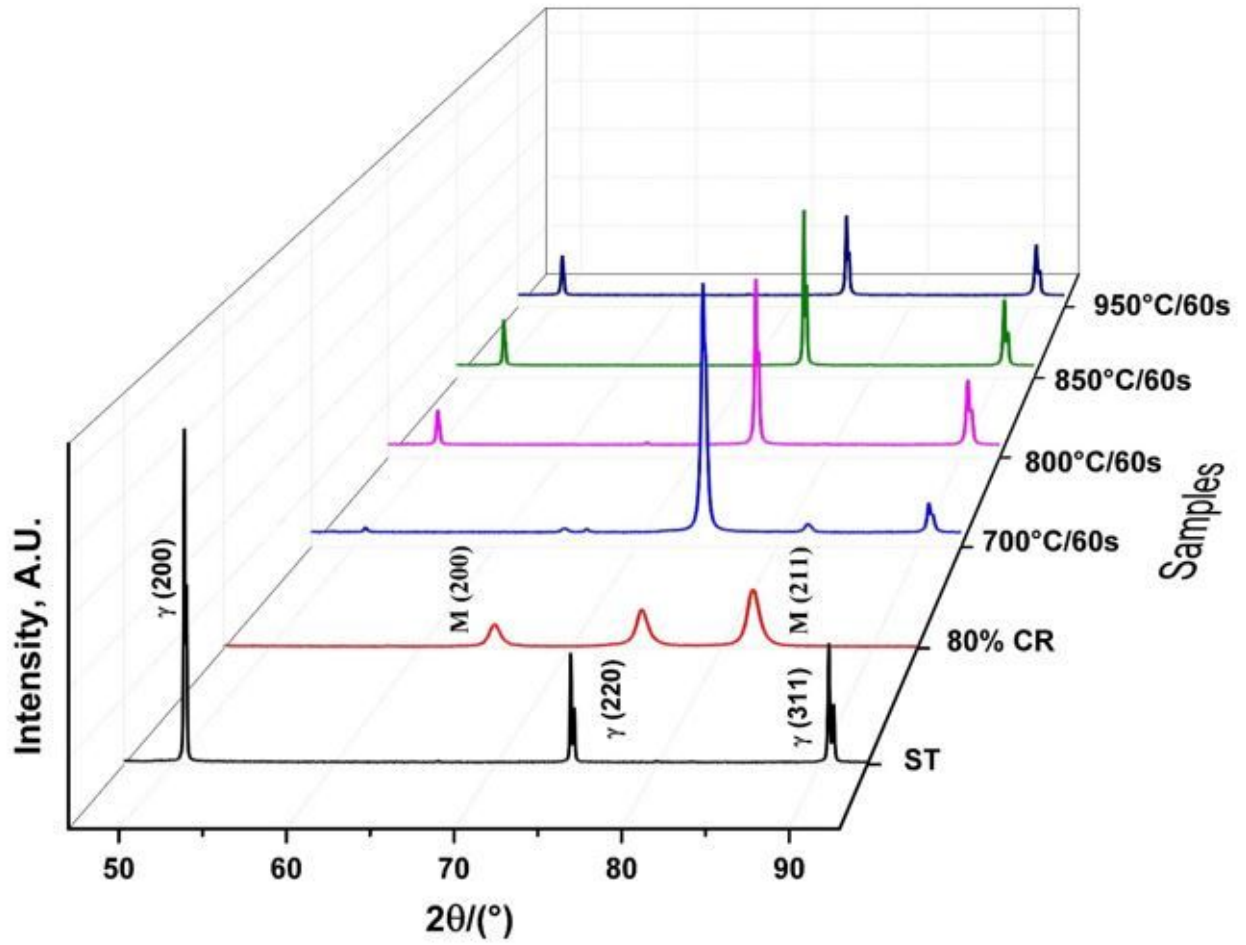


Figure 1

The XRD patterns for each stage of the treatment.

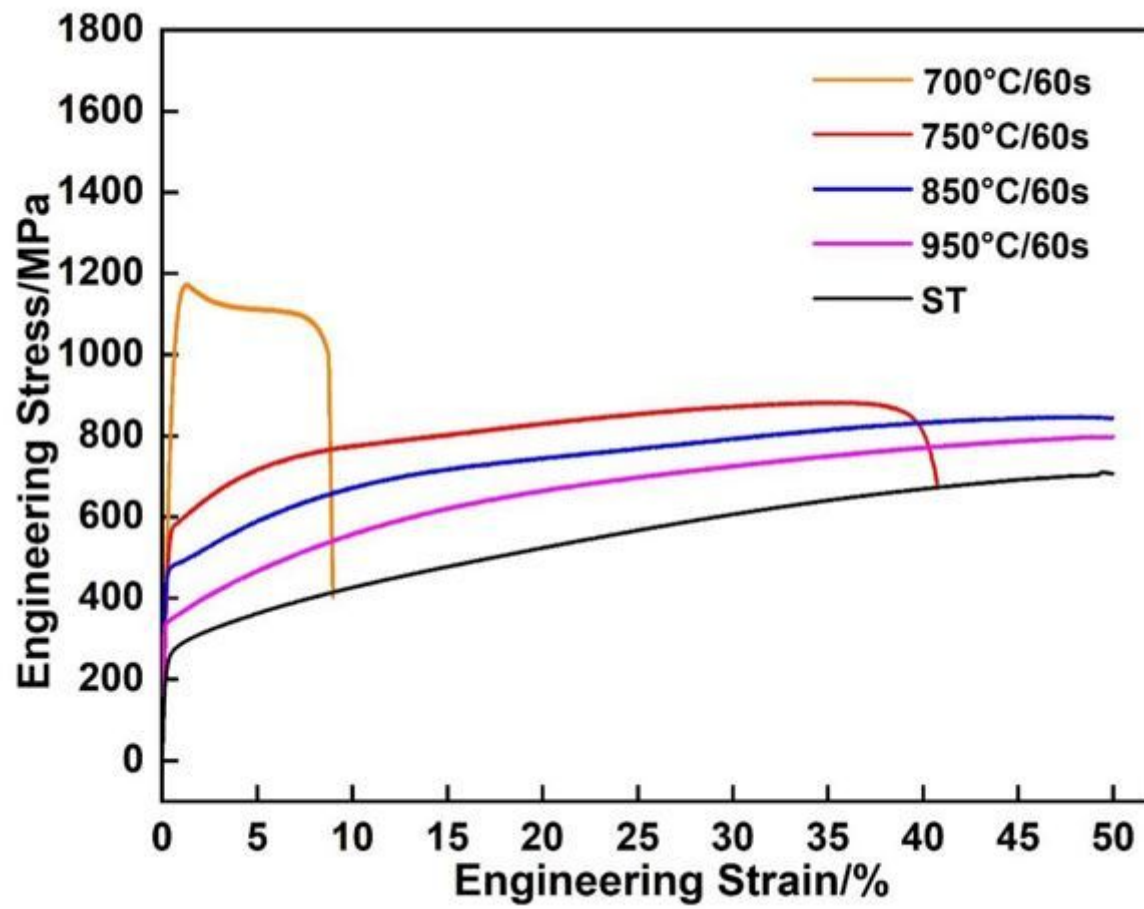


Figure 2

Engineering stress-strain tensile curves for austenitic stainless steel.

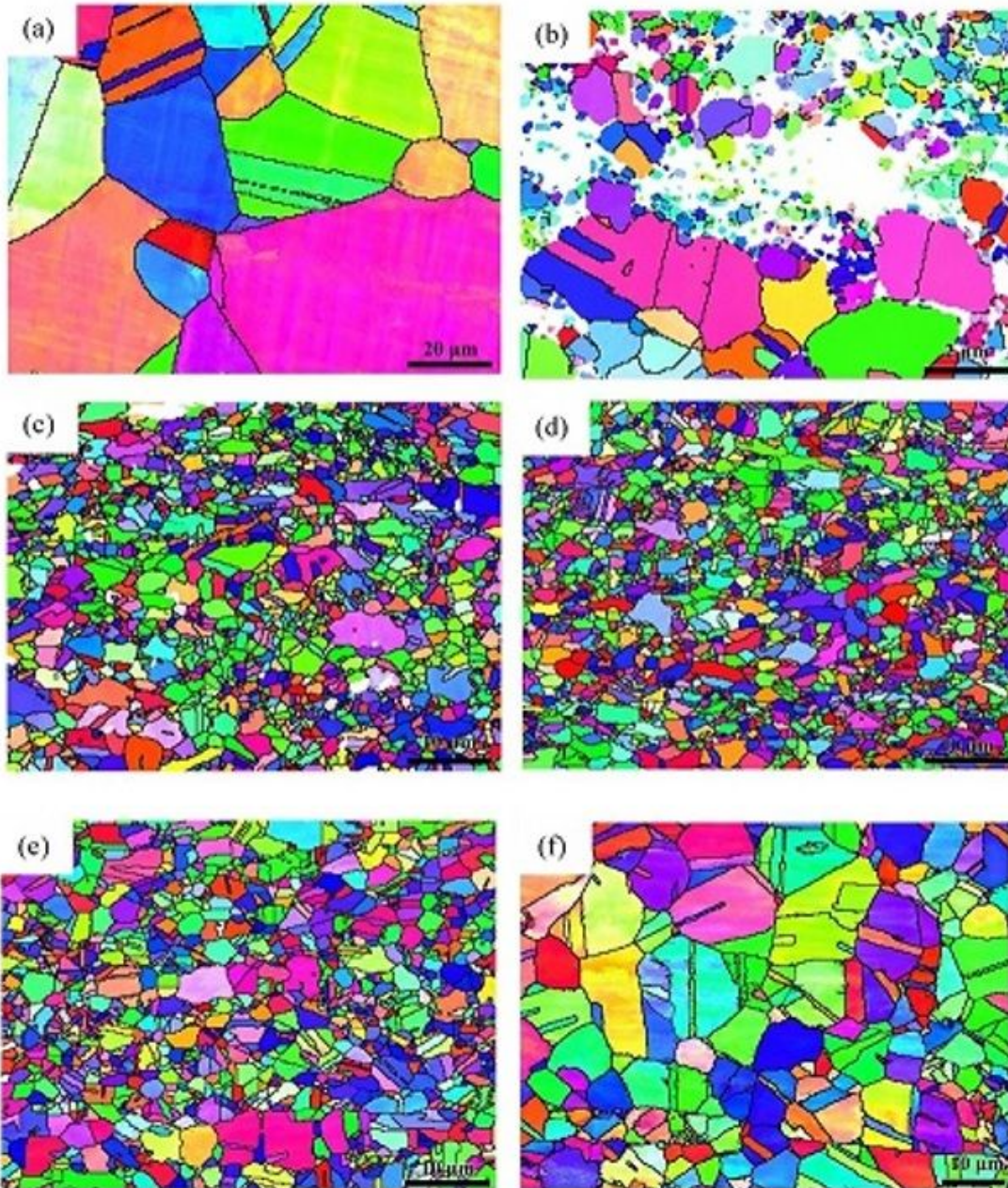


Figure 3

EBSD maps of austenitic stainless steels (a) after solution treatment and annealed at (b) 700 °C, (c) 750 °C, (d) 800 °C, (e) 850 °C (f) 950 °C for 60s.

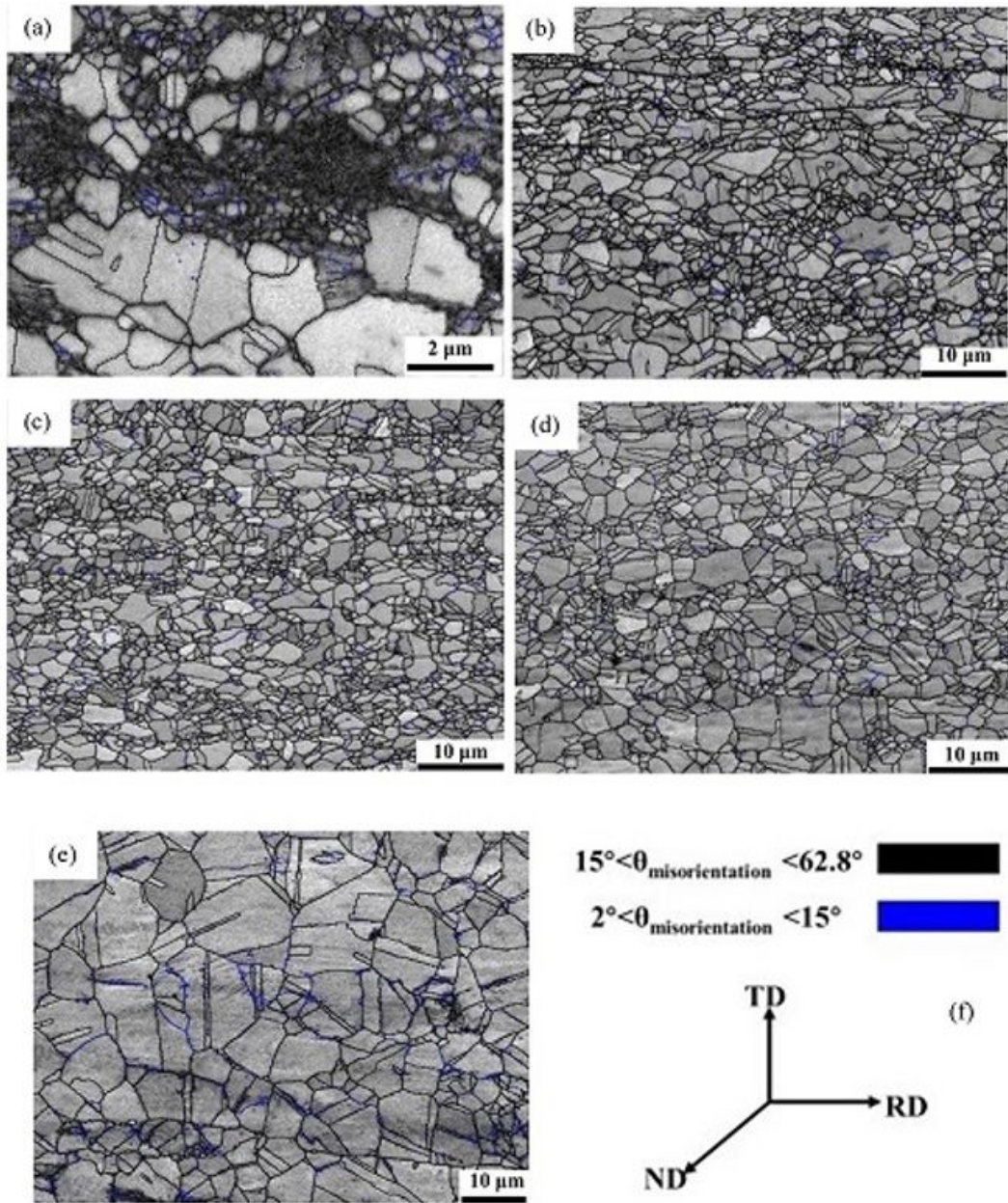


Figure 4

EBSD band contrast maps with grain boundary misorientation distribution of austenitic stainless steels annealed at (a) 700 °C, (b) 750 °C, (c) 800 °C, (d) 850 °C (e) 950 °C for 60s, (f) misorientation angles.

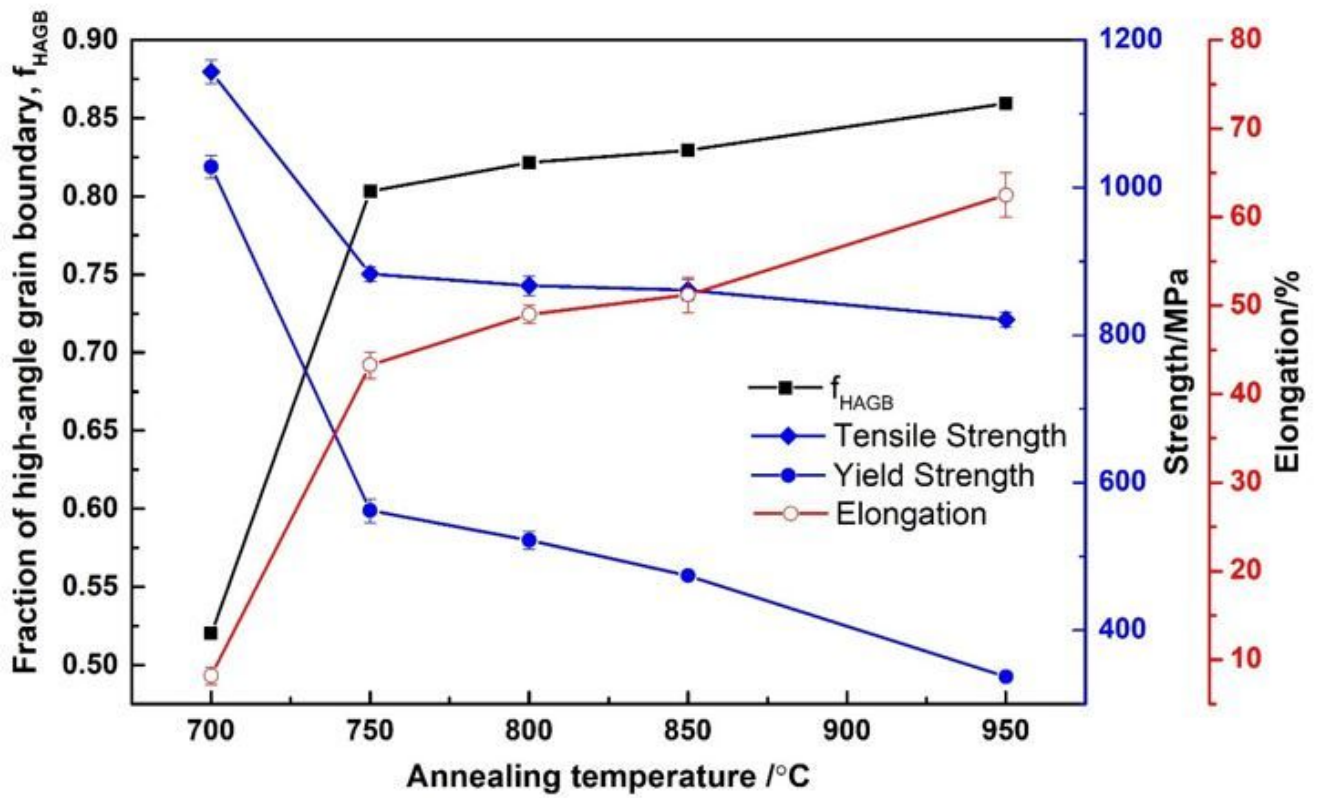


Figure 5

Fractions of HAGBs and mechanical properties of austenitic stainless steels annealed at different temperatures.

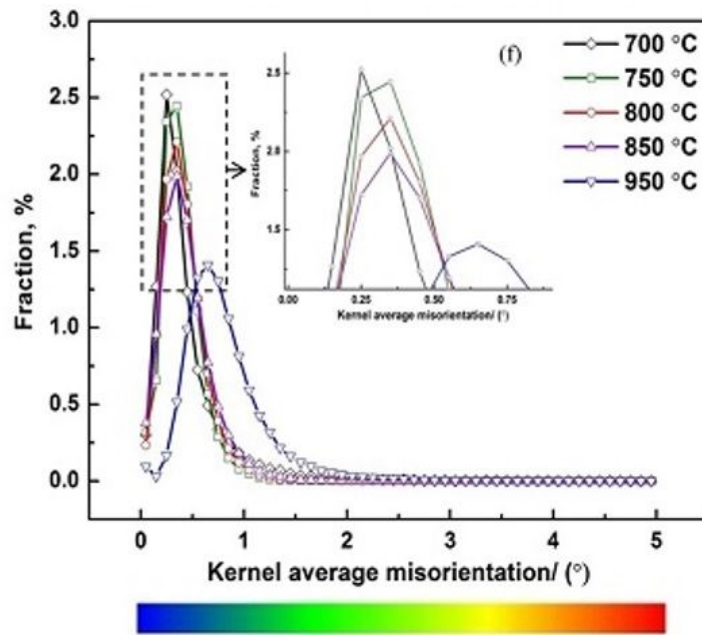
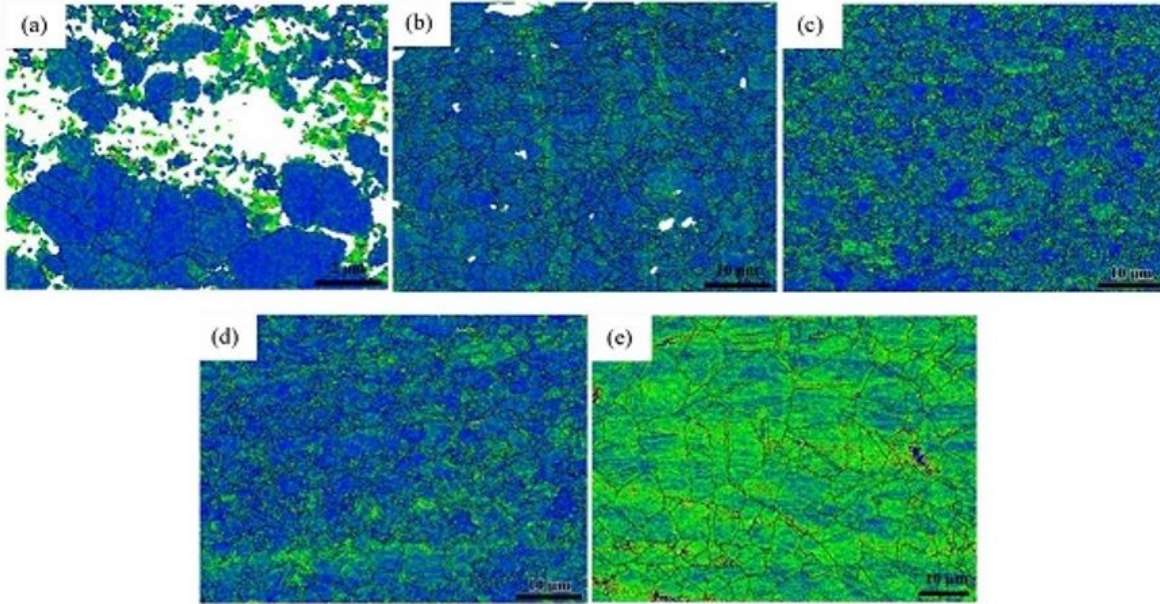


Figure 6

KAM distribution maps of austenitic stainless steels annealed at (a) 700 °C, (b) 750 °C, (c) 800 °C, (d) 850 °C (e) 950 °C for 60s, and (f) the distribution of KAM values at different annealing temperatures.

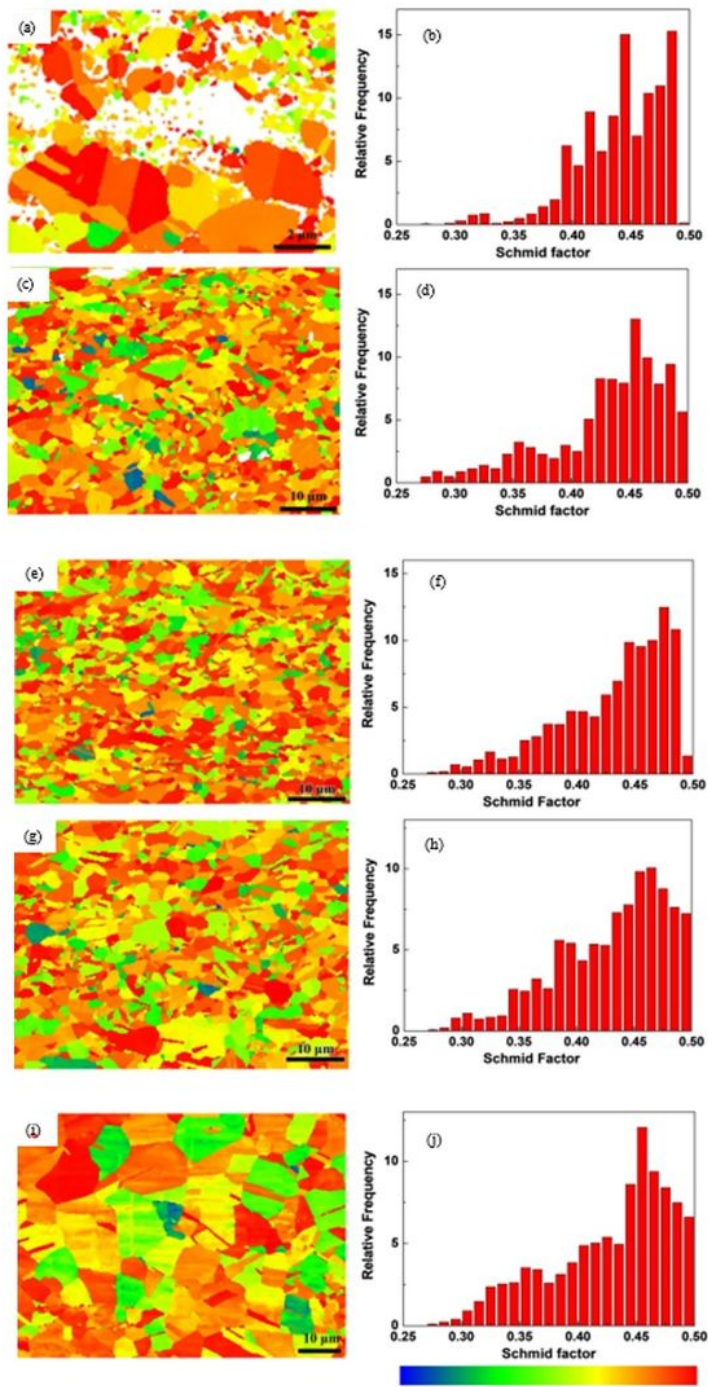


Figure 7

Schmid factor of austenitic stainless steels annealed at (a) and (b) 700 °C, (c) and (d) 750 °C, (e) and (f) 800 °C, (g) and (h) 850 °C (i) and (j) 950 °C for 60s.

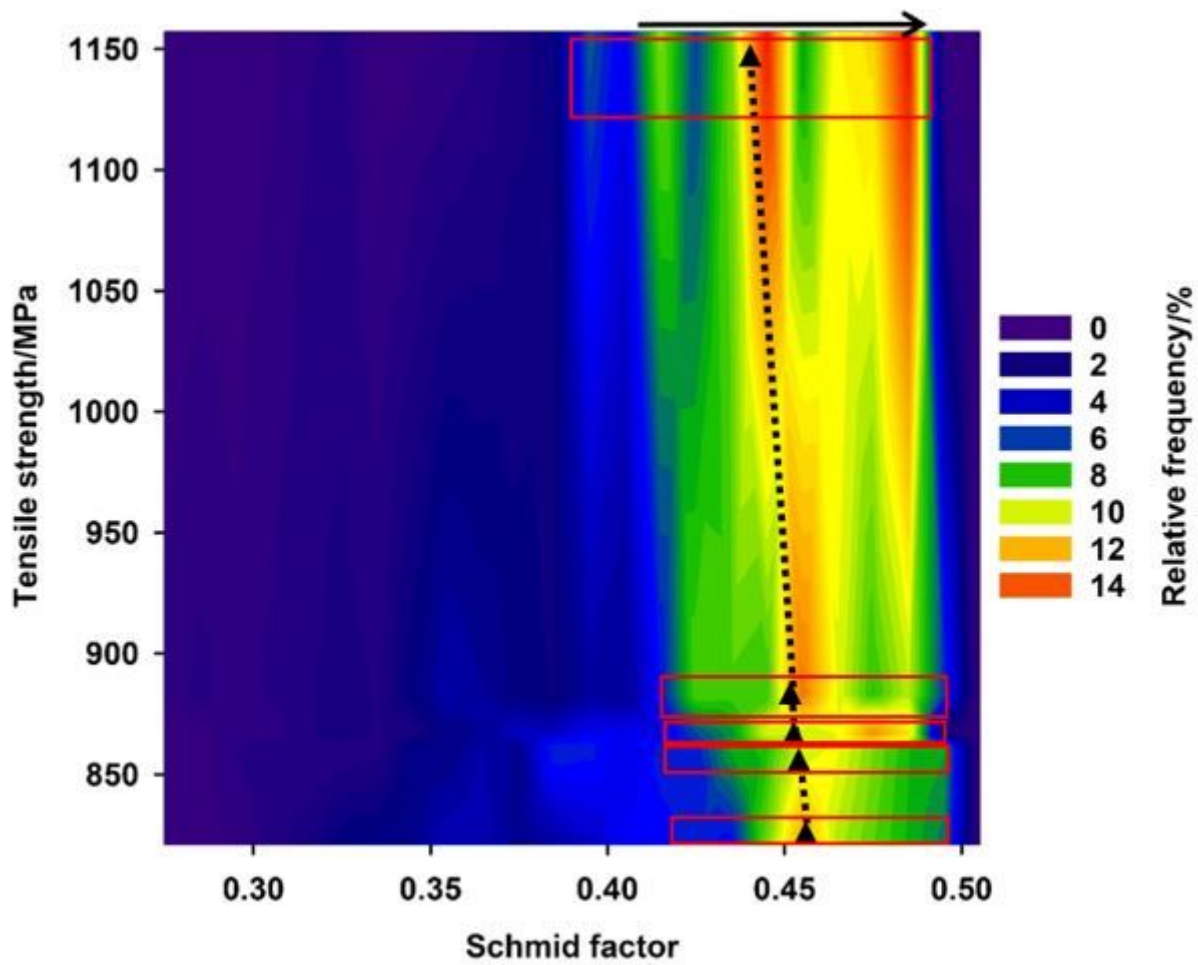


Figure 8

Contour Map of Schmid factor distributions for annealed austenitic stainless steels associated with tensile strength (Triangle: weighted arithmetic mean of Schmid factor after getting rid of Schmid factor frequency lower than 5%).

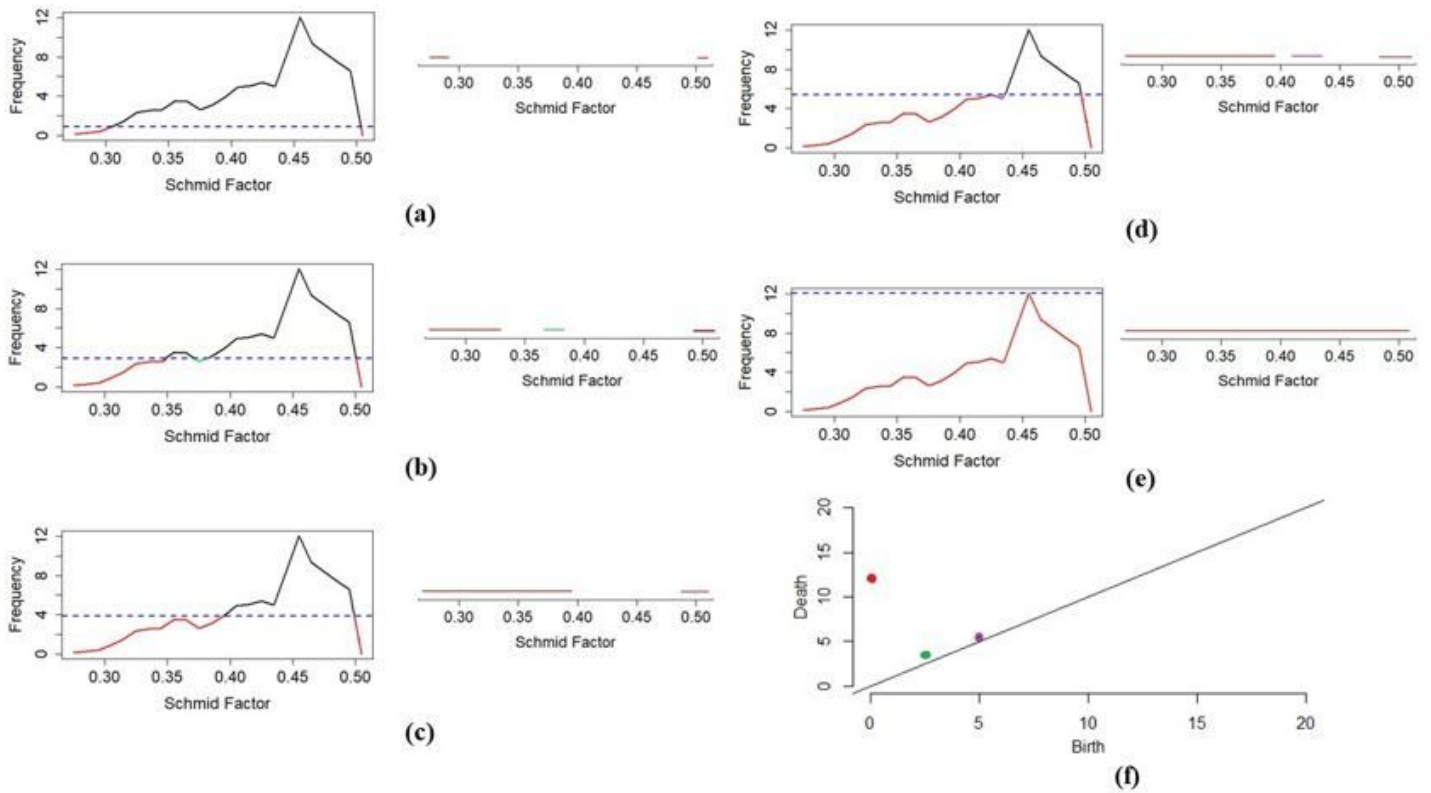


Figure 9

The step-by-step construction of persistence diagram from the frequency plot of Schmid factor at an annealing temperature of 950 °C summarizing the birth and death scale of connected components of sublevel sets. (a) Birth of two red connected components; (b) Birth of green connected component; (c) Death of green connected component; (d) Birth of purple connected component; (e) Death of the rest of connected component; (f) Persistence diagram of all connected components.

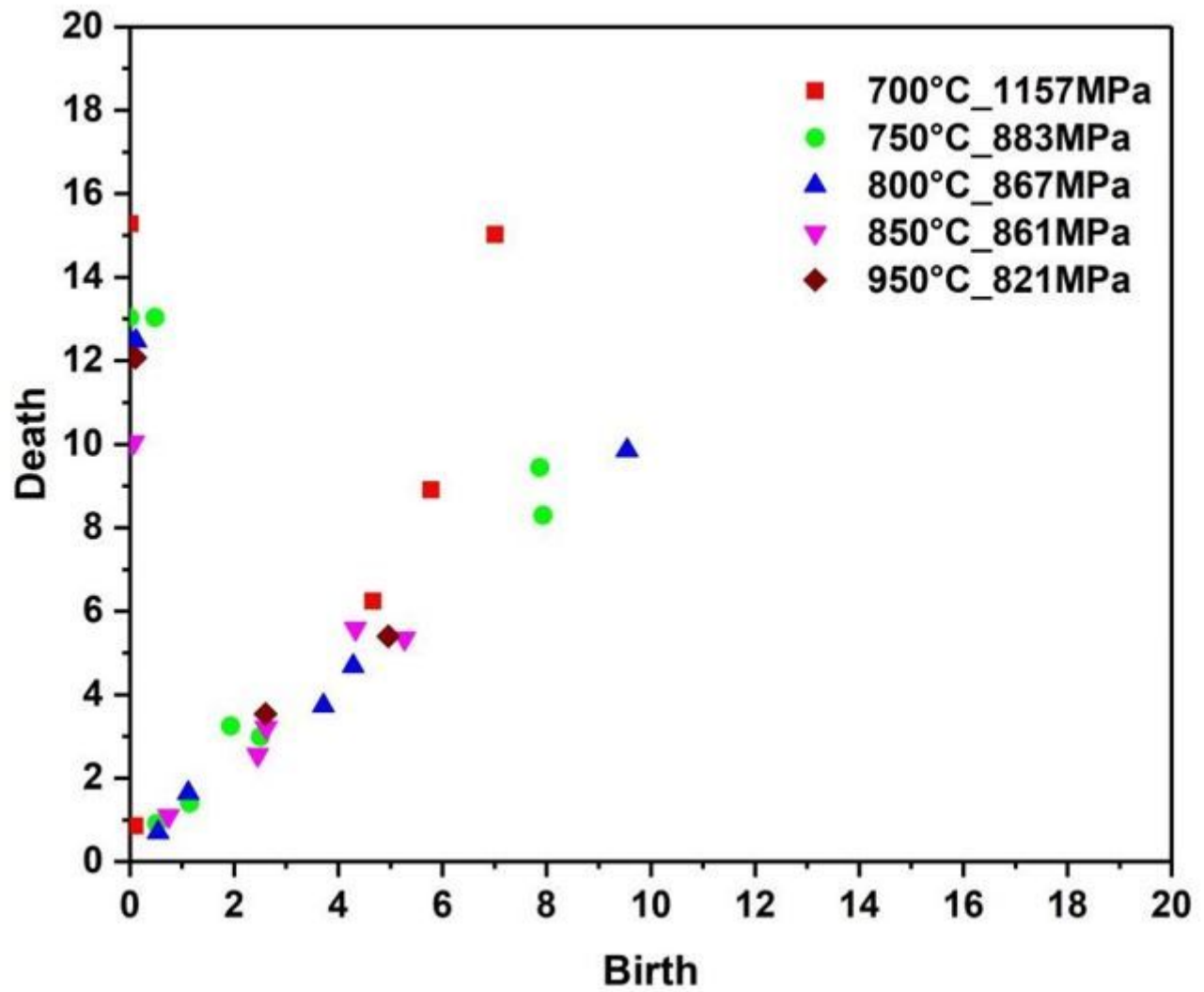


Figure 10

The combined PD plot for several frequency distributions of Schmid factors in varying annealing temperature levels.

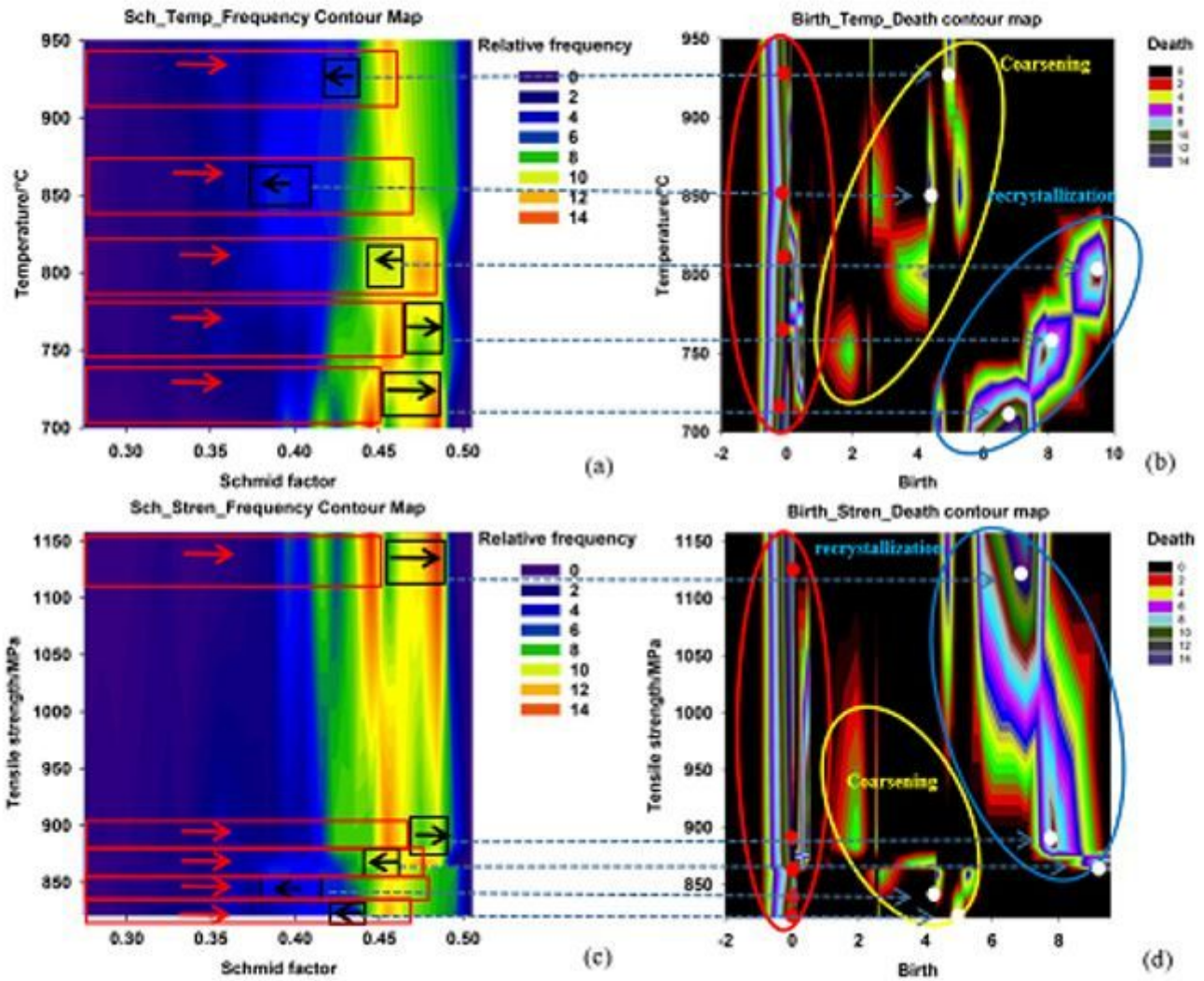


Figure 11

Contour maps of (a) Schmid factor, temperature and frequency; (b) Schmid factor, strength and frequency; (c) birth, temperature and death; (d) birth, strength and death, representing the correlation of Schmid factor frequency distribution and PDs.